Polycarbazole Nanocomposites with Conducting Metal Oxides for Transparent Electrode Applications

Katsuyoshi Hoshino,*,† Naoki Yazawa,† Yoshiyasu Tanaka,† Takeshi Chiba,† Takenori Izumizawa,‡ and Minako Kubo‡

Graduate School of Advanced Integrated Science, Chiba University, 1-33 Yayoi, Inage, Chiba 263-8522, Japan, and Goi Research Center, Chisso Petrochemical Company, 5-1 Goikaigan, Ichihara, Chiba 290-8551, Japan

ABSTRACT The preparation and characterization of conducting polycarbazole (PCz) hybrid films with a colorless transparency are described. They were prepared by the vacuum evaporation of tin, aluminum, or gallium onto anion-doped green-colored PCz films, or by applying gallium to the films, followed by their exposure to ambient air. The resultant hybrid films consisting of an undoped PCz backbone and metal compounds exhibited good transparencies (90−95% at a wavelength of 550 nm). The hybrid films have a specific cross-sectional structure in which the small regions of the metal compounds are dispersed in the PCz backbone. The hybridization reaction was mechanistically explained on the basis of the combination of a metal corrosion reaction and polymer dedoping reaction, which was successfully supported by the chemical analyses of the hybrid films. The electric conductivities of the hybrid films, measured by a four-point-probe method, ranged from 2.2×10^{-4} to 6.0×10^{-3} S cm^{-1}, which are considered to be the lowest limit because the use of the hybrid films as an electrochemical electrode reveals that a network of conductive paths is preferentially formed in the film thickness direction rather than in the in-plane direction.

KEYWORDS: conducting metal oxides • polycarbazole • nanocomposites • transparent electrode • cyclic voltammetry

1. INTRODUCTION

Transparent conducting materials are indispensable for use as transparent electrodes in flat panel displays such as liquid crystal displays (LCDs), plasma displays, electronic papers, and organic electroluminescent displays, and for electrode applications in thin-film solar cells and touch panels (1). As the main materials, indium−tin-oxides (ITOs) have been used in most of these transparent electrode applications. However, one of the constituents of the ITO, indium (In), is a rare metal, and hence, the rising demand of the ITO is widely believed to cause an In shortage in the near future (1−3). This resource availability problem motivated material scientists to find alternatives to the ITO and/or to find a recovery process (4) for In from LCDs because ca. 84% of the global indium consumption (5) is used for the production of LCDs. In this context, polymer composites with nanosized fillers have attracted much attention because of their feasibility for use as electrically conductive materials with good optical transparencies. A recent study on the use of carbon nanotubes (CNT) as a filler (6−14) revealed that the typical CNT-filled polymer films exhibit an electric conductivity of $\sim 1 \times 10^{-3}$ S cm^{-1} and optical transmittance of 90% at 550 nm (14). These combined properties of good electric conductivity and transparency are likely based on the high electric conductivity of the CNTs and the high aspect ratio of the CNTs which enables their reduced use in the composite.

The CNT-filled polymer materials have a good flexible nature due to their flexible polymer backbone, and therefore, are compatible with transparent electrodes for the next-generation flexible devices such as organic electroluminescent displays, electronic papers, organic solar cells, etc. This might be considered as an advantage over the rigid candidates under development such as CNT(or carbon nanographite)-filled SiO_2 (15−17), aluminum zinc oxide (2, 3), gallium zinc oxide (2, 3), etc. Additionally, another notable feature of the CNT-filled composites is their enhanced mechanical strength compared to the CNT-free polymer materials. This enhancement is considered to be based on the nucleophile−electrophile interaction between the CNT and polymer materials (18, 19). This mechanical feature distinguishes the CNT-filled composites from the transparent conducting polymer materials (20−29) currently under development, being one of the features of technological importance. The approach using CNT−polymer composites is thus promising for the preparation of electrically conductive materials with a good transparency.

However, there are serious problems in the preparation of CNT-dispersed polymer solutions and their coating procedures. CNTs are liable to aggregate by van der Waals interactions, so that the difficulty is found in dispersing them in the polymer solution, and exposure of the dispersion to shear during the coating leads to aggregation (14).

On the other hand, we have developed a simple strategy to prepare novel aluminum-compound-containing conduct-

* To whom correspondence should be addressed. Fax: +81-43-290-3478. E-mail: k_hoshino@faculty.chiba-u.jp.

Received for review October 8, 2009 and accepted January 20, 2010

† Chiba University.

‡ Chisso Petrochemical Co.

DOI: 10.1021/am900684e

ing polymer films. This strategy involves the vacuum evaporation of an aluminum film on the conducting polymer film, followed by its exposure to ambient atmosphere. During the exposure, a solid-state cell reaction spontaneously occurs between the two films to form the composite film. This composite film is characterized by its unique nanostructure in which the nanoparticles of aluminum compounds are dispersed in the polymer matrix film.

This novel approach based on the cell reaction is similar to that using the CNT-filled composites in that nanosized fillers are dispersed in the polymer backbone, but is quite different in that the fillers are spontaneously formed and dispersed in the polymer film bulk, and no aggregation occurs during the formation process. The first approach is the preparation of a composite material using the combination of polypyrrole and aluminum (30). However, the composite was intensely colored despite its high electric conductivity. The second is based on the composite material prepared by the reaction of polycarbazole (PCz) with aluminum (31). This composite showed a good colorless transparency, but the electric conductivity of the film is decreased by the reaction, thus preventing its use as a transparent conducting material.

In this study, we report the finding that electrically conductive composite materials with a good transparency are formed by the cell reaction between PCz and tin (or gallium). The conductivity of the composite is higher than (or comparable to) the as-grown PCz single film. In addition, the applications of the composite films as an electrochemical electrode material will be described.

2. EXPERIMENTAL SECTION

2.1. Electropolymerization. The PCz films were prepared on an ITO-coated glass plate (ITO, Geomatech, 10 Ω/sq) and a stainless plate (Nilaco Co., SUS-304) by the electro-oxidation of 5 mM carbazole (Tokyo Kasei Kogyo, 98%) dissolved in a dichloromethane solution containing tetrabutylammonium perchlorate (TBAP, >98%, 0.1 M) at 20 °C under an N_2 atmosphere using an electrochemical analyzer (BAS Co., ALS model 750A) (31). The stainless plate was chosen because it is indium-free and more representative of engineering materials. The working electrode (ITO or stainless plate) and the counter Pt plate were immersed in the main compartment of the electrolysis cell. Prior to the electrolysis, the ITO (or stainless) and Pt plates were ultrasonically washed in distilled−deionized water and then in acetone for 10 min each. In the auxiliary compartment, which is separated from the main one by a sintered glass frit, was immersed a KCl agar bridge connected to the reference saturated calomel electrode (SCE, BAS Co.). The controlled-potential electro-oxidation at +1.2 V vs SCE provided green-colored ClO_4^--doped PCz films on the ITO (or stainless plate). The thickness of the film showed a linear dependence on the amount of electricity (Q) passed through a unit area of the ITO, 16 nm per 1 mC cm^{-2}. The resultant PCz films were washed with dichloromethane and dried in air.

2.2. Vacuum Evaporation. Films of Sn (99.9%, Nilaco Co.) and Ga (99.9999%, Nilaco Co.) were deposited on the PCz films at room temperature by thermal evaporation under a vacuum of $\sim 8 \times 10^{-3}$ Pa using a vacuum coating apparatus (ULVAC, model VPC-260F). The metal film thickness (L) was controlled during the evaporation process via a quartz crystal thickness monitor (ULVAC, model CRTM-6000).

2.3. Sample Characterization. The morphology of the hybrid films was investigated by transmission electron (TEM, Hitachi FE-TEM HF-2200) and scanning electron microscopic (SEM, Topcon ABT-32) observations. The cross-sectional sample for the TEM observations was prepared as follows. A protective layer of carbon was evaporated on the hybrid films. A transversally cut slice was prepared by milling with gallium ions at 30 kV. X-ray photoelectron spectroscopy (XPS, ULVAC phi ESCA 5400 spectrometer with Al Kα radiation) and energy-dispersive X-ray analysis (EDX, Noran Vantage EDS system) were employed for the compositional analyses of the sample films. The absolute binding energy scale in the XPS was determined by setting the C 1s signal to 284.6 eV.

2.4. Reaction Using Molten Metals. A hybridization reaction of the PCz with gallium metal simply occurred by applying molten gallium to the PCz film surface in a constant-temperature oven (Yamato, Constant temperature oven DN64) at temperatures above 35 °C. Care must be taken to remove the surface native oxide layer of gallium during the contact since no hybridization reaction occurs in the presence of the oxide layer. To enlarge the contact area between the PCz film and gallium, a slide glass was placed on the molten gallium to apply pressure. After the completion of the reaction, the sample was taken out of the oven and any excess gallium was removed from the PCz film surface.

2.5. Electric Conductivity Measurements. The electric conductivity of the films, σ, was measured by the usual four point probe method (Mitsubishi Chemical Analytech Co., Loresta-GP MCP-T600 and MCP-TP06P probe). The test samples were prepared as follows. The PCz and its hybrid films prepared on the ITO (or stainless) plates were dipped in a binder polymer solution consisting of polycarbonate (Teijin Chemicals Panlite K-1300Y, resistivity $\geq 1 \times 10^{15}$ Ω cm), dichloromethane, and chloroform (1:8:8 weight ratio). The samples were then pulled out of the solution and dried at 60 °C for 3 h. The resultant films covered with the polycarbonate layer were stripped from the ITO (or stainless) plate and subjected to the conductivity measurements. Electric conductivity measurements were also carried out using evaporated gold electrodes, the details of which will be described in the text (section 3.3).

2.6. Electrochemical Measurements. The PCz/Sn (or Al) hybrid film (10 mm × 10 mm × 0.4 μm) back-coated with polycarbonate (see section 2.5) was mounted on a polyester (Toyobo Co., Vylon 200)-coated glass plate just after coating the plate with a polyester solution containing polyester resin, toluene, and tetrahydrofuran in the weight ratio of 1:3:3, followed by drying at 40 °C for 1 h. A part of the surface of the PCz/Sn (or PCz/Al) film electrodes was then coated with gold by vacuum evaporation, and a copper wire was fixed to the gold surface by silver paste. Schematic diagrams of the electrode structures are shown in Figures 6 and 9. The prepared PCz/Sn (or PCz/Al) electrode was placed in an acetonitrile solution containing 1 mM ferrocene (Fc, Tokyo Kasei Kogyo, 98%) and 0.1 M tetrabutylammonium perchlorate (Tokyo Kasei Kogyo, >98%, abbreviated as TBAP), and the electrochemical response of ferrocene was measured by cyclic voltammetry.

3. RESULTS AND DISCUSSION

3.1. Reaction Model. Our previous finding of the hybridization reaction using aluminum metal motivated us to use alternative metals since the type of metal is expected to affect the kinetics of the reaction and the physicochemical properties of the resulting hybrid films. Figure 1 shows the time (t)-dependent change in the UV−vis absorption spectra of PCz films (0.4 μm thick) in contact with a vacuum-evaporated Sn film (11 nm thick) (a), vacuum-evaporated Ga film (6 nm thick) (b), vacuum-evaporated Al film (6 nm thick)

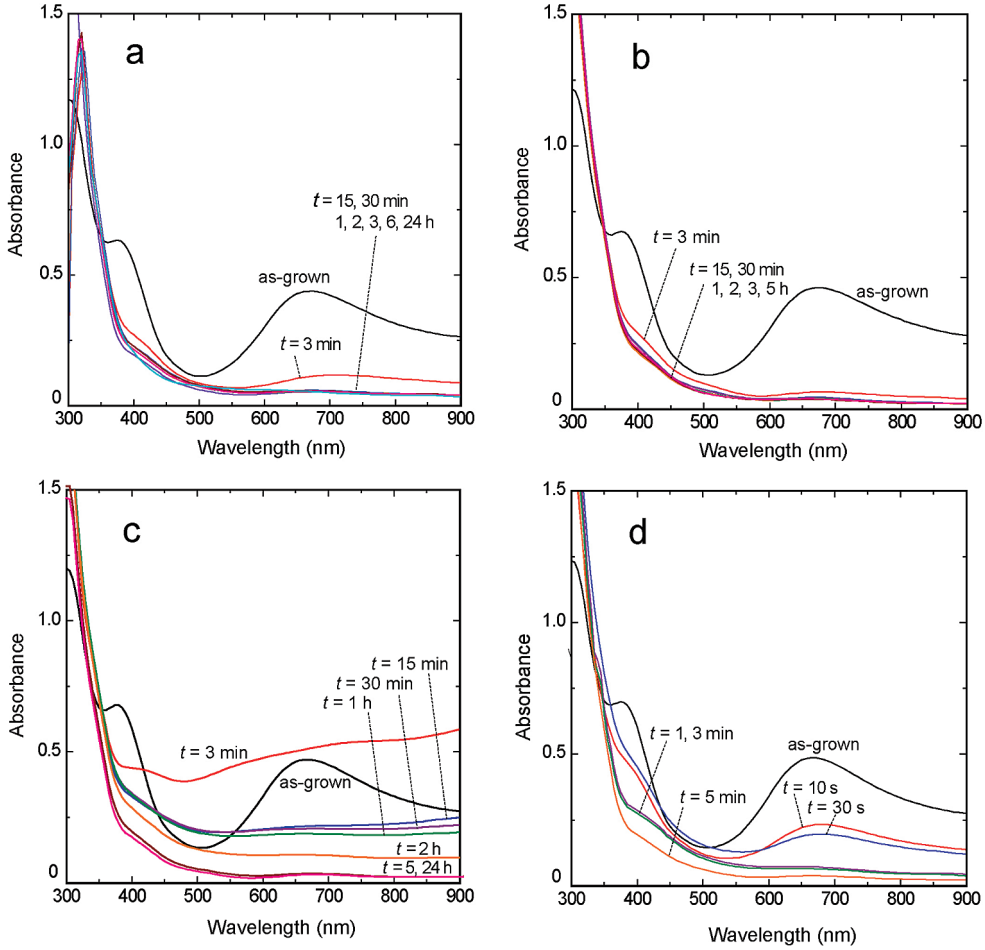

FIGURE 1. Time-dependent change in UV−vis absorption spectra during the hybridization reaction occurring in (a) PCz(0.4 μm)/Sn(11 nm), (b) PCz(0.4 μm)/Ga_f(6 nm), (c) PCz(0.4 μm)/Al(6 nm), and (d) PCz(0.4 μm)/Ga_m films. Each part involves the spectrum of the as-grown PCz film (0.4 μ m thick) for comparison purposes.

(c), and Ga metal mass (d). The numerals in the figures show the time, *t*. The Ga metals in the form of a film and mass are hereinafter abbreviated as Ga_f and Ga_m, respectively. For the evaporated metals (Al, Sn, and Ga_f), time was measured after the samples were taken out of the vacuum chamber in which the metals were evaporated; the hybridization reaction was initiated by the exposure of the samples to air as no reaction occurred in a vacuum. For the Ga_m, its contact time with the PCz film was employed. The ambient temperature during the contact was 40 °C. The result for the PCz/Al system was previously reported (31), but it was checked again for reproducibility and comparison purposes. As was evidenced by the time-dependent decrease in the specific absorptions at 680 and 380 nm, all the metals reacted with the PCz film to produce transparent hybrid films. The absorptions were previously assigned to the oxidized carbazole unit in the PCz (32, 33).

These observations are quite similar to that for the previously reported PCz/Al film (31), and according to the report, the reaction demonstrated by Figure 1 is explained on the basis of the following modified galvanic corrosion reaction. When the metals come into contact with the perchlorate-doped PCz film, the junction with a large work-function (ϕ) difference is formed between the PCz film (ϕ = 5.5 eV (31)) and the metals (34): ϕ for Sn, 4.42 eV; ϕ for Ga, 4.2 eV; ϕ for Al, 4.28 eV. Under ordinary pressure and temperature, adsorbed water (35, 36) should cover the junction and intervene between the two materials at the sites with structural defects, such as microcracks, microscratches, and pinholes. At such sites, the electropositive PCz film may give rise to a local corrosion cell with the electronegative metals, and electron transfer from the latter to the former occurs that is driven by the difference in their work functions. The anodic oxidation of metal to metal ions is followed by its conversion to the corresponding oxide/hydroxide and the perchlorate salt. The cathodic reactions involve the reduction of the cationic species in the PCz film (polarons and/or bipolarons) and the reduction of protons that form along with metal oxide/hydroxide during the corrosion reaction in natural environments (36−38). The former reduction causes the release of ClO_4^- from the PCz backbone (dedoping), and the resultant ClO_4^- is coupled with the metal ion to form a perchlorate salt.

The formation of a metal oxide and salt in the above reaction process was evidenced by the XPS analyses of the PCz/Ga_f hybrid system. The authentic samples of Ga_2O_3 (Wako pure chemical Co., 99.99%) and $Ga(ClO_4)_3 \cdot xH_2O$ (Aldrich, 99.999%) are commercially available, allowing us to compare the Ga 2p3/2 signals of these authentic compounds with that in the PCz/Ga_f system. Figure 2 shows the

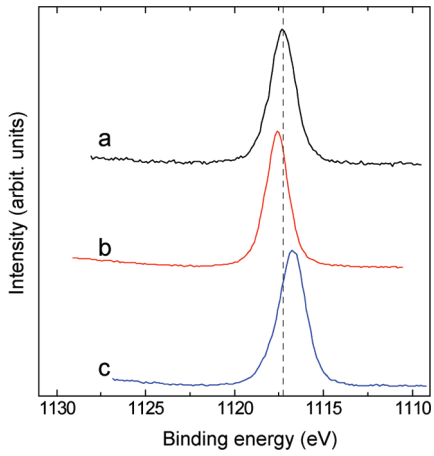

FIGURE 2. XPS spectra in the Ga 2p3/2 region for the (a) PCz(0.4 μm)/Ga_f film, (b) Ga_2O_3 powder, and (c) $Ga(ClO_4)_3$ powder.

Ga 2p3/2 signals of the PCz/Ga_f film (a), Ga_2O_3 powder (b), and $Ga(ClO_4)_3$ powder (c). The peak position of curve a (1117.30 eV) locates between those of curves b (1117.58 eV) and c (1116.85 eV), suggesting that the gallium compound in the film is the mixture of Ga_2O_3 and $Ga(ClO_4)_3$. If this is assumed, their concentration ratio in the film can be calculated using the atomic concentrations of Cl and Ga. The XPS analyses of the Cl 2p and Ga 2p3/2 signals at three different points on the PCz/Ga_f film revealed that the average concentration ratio of Ga_2O_3 and $Ga(ClO_4)_3$ is 50:50.

According to the above reaction model, the transparency of the hybrid films may be determined by the amount of the metal in contact with the PCz film. Indeed, plot of the absorbance versus the evaporated metal film thickness shows minimum at a given thickness (critical film thickness, CFT) for the PCz(0.4 μm)/evaporated metal hybrid films (see section 3.4). Below the CFT, the hybrid films are colored green, with the green film being gradually bleached with the increasing metal film thickness. Above the CFT, an excess amount of metal, not taking part in the hybridization reaction, remained in the PCz film, making the film opaque gray. The CFT values for the PCz(0.4 μm)/metal (metal = Sn, Ga_f, and Al) films were 11, 6, and 6 nm, respectively. In the case of the stoichiometric PCz(0.4 μm)/Ga_f hybrid system, the number of gallium atoms in the 6 nm thick Ga film per unit area, N_{Ga}, was determined to be 3.1×10^{16} cm^{-2} using the density (5.904 g cm^{-3}) (39) and the atomic weight (69.72 g mol^{-1}). The value of Q is the total charge consumed in the polymerization of carbazole and the doping of ClO_4^- in the generated PCz film. The former and the latter amounts are given by $2(n-1)e$ and xne, respectively, where n, x, and e denote the number of carbazole units involved in the PCz film per unit area, the doping level of the PCz film, and elementary charge, respectively.

$$Q = 2(n-1)e + xne \quad (1)$$

This relationship allowed us to calculate the value of n, 6.0×10^{16} cm^{-2}, and the number of ClO_4^-, $xn = 2.9 \times 10^{16}$ cm^{-2}, for the 0.4 μm thick PCz film using the value of x (= 0.49) determined by the XPS measurements and the amount of Q (= 24 mC cm^{-2}). If we assume that the Ga atoms are consumed by the dedoping and the corrosion reactions, the following relationships can be expected to hold

$$\frac{xn}{3}\mathrm{Ga} + \mathrm{PCz}^{xn+}(\mathrm{ClO_4^-})_{xn} \rightarrow \frac{xn}{3}\mathrm{Ga(ClO_4)_3} + \mathrm{PCz} \quad (2)$$

$$\left(N_{Ga} - \frac{xn}{3}\right)\mathrm{Ga} + 3\left(N_{Ga} - \frac{xn}{3}\right)\mathrm{H_2O} \rightarrow \frac{1}{2}\left(N_{Ga} - \frac{xn}{3}\right)\mathrm{Ga_2O_3 \cdot 3H_2O} + \frac{3}{2}\left(N_{Ga} - \frac{xn}{3}\right)\mathrm{H_2} \quad (3)$$

Equation 2 shows the complete reduction of the ClO_4^--doped PCz, $PCz^{xn+}(ClO_4^-)_{xn}$ by the action of Ga to form $Ga(ClO_4)_3$ and the undoped PCz. The rest of the evaporated Ga is corroded to form $Ga_2O_3 \cdot 3H_2O$ (36−38) according to eq 3. These assumptions allowed us to estimate the fractions of Ga atoms taking part in the dedoping reaction, 32%, and those in the corrosion reaction, 68%. This result, in turn, provides the mole ratio of the reaction products, Ga_2O_3:$Ga(ClO_4)_3$ = 51:49. This ratio is in good agreement with that determined by the XPS analyses, 50:50, shown above.

Also, in the case of the PCz(0.4 μm)/Al(6 nm) system, the concentration ratio of the reaction products, Al_2O_3:$Al(ClO_4)_3$, can be calculated on the basis of the treatments analogous to eqs 1, 2, and 3. Thus, the ratio was calculated as 57:43 using the density (2.70 g cm^{-3}) (39) and the atomic weight (26.98 g mol^{-1}). This value agrees well with that measured by the XPS of the Al 2p and Cl 2p signals, 56:44. In addition, the fractions of Al atoms participating in the dedoping reaction and the corrosion reaction were 27 and 73%, respectively.

For the treatment of the PCz(0.4 μm)/Sn(11 nm) system, eqs 2 and 3 should be replaced by eqs 4 and 5.

$$\frac{xn}{4}\mathrm{Sn} + \mathrm{PCz}^{xn+}(\mathrm{ClO_4^-})_{xn} \rightarrow \frac{xn}{4}\mathrm{Sn(ClO_4)_4} + \mathrm{PCz} \quad (4)$$

$$\left(N_{Sn} - \frac{xn}{4}\right)\mathrm{Sn} + 4\left(N_{Sn} - \frac{xn}{4}\right)\mathrm{H_2O} \rightarrow \left(N_{Sn} - \frac{xn}{4}\right)\mathrm{SnO_2 \cdot 2H_2O} + 2\left(N_{Sn} - \frac{xn}{4}\right)\mathrm{H_2} \quad (5)$$

On the basis of the treatments using eqs 1, 4, and 5, the concentration ratio of SnO_2 and $Sn(ClO_4)_4$ was calculated to be 82:18. This value was again supported by the experimental value of the XPS measurement of the Sn 3d and Cl 2p signals, 88:12. The fractions of Sn atoms converted to SnO_2 and $Sn(ClO_4)_4$ were 82 and 18%, respectively. The above mechanistic considerations and compositional analyses of the hybrid films support our previously assumed reaction model (31) in which the dedoping of the PCz and the corrosion reaction simultaneously occurs.

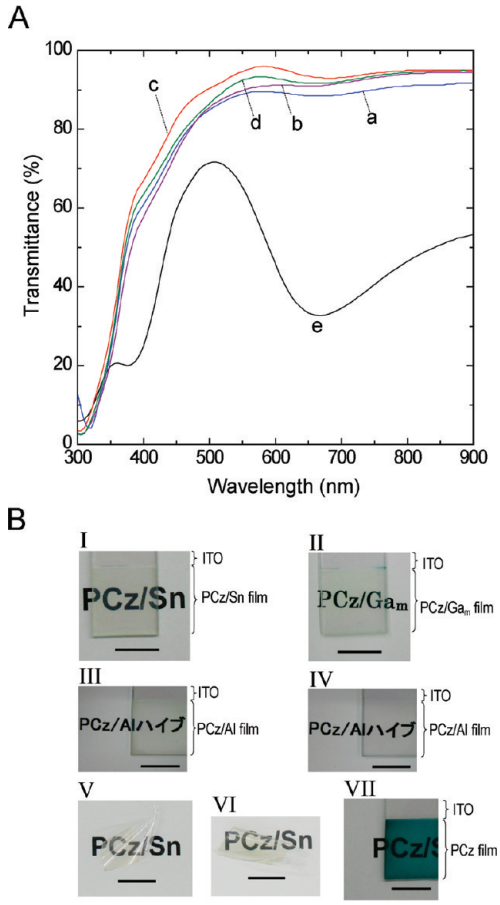

FIGURE 3. Data showing the transparent features of the hybrid films. (A) UV−vis transmission spectra of (a) PCz(0.4 μm)/Sn(11 nm), (b) PCz(0.4 μm)/Ga$_f$(6 nm), (c) PCz(0.4 μm)/Al(6 nm), and (d) PCz(0.4 μm)/Ga$_m$ hybrid films. (B) Photographs of (I) PCz(0.4 μm)/Sn(11 nm), (II) PCz(0.4 μm)/Ga$_m$, (III) PCz(0.4 μm)/Al(6 nm), (IV) PCz(0.2 μm)/Al(3 nm), (V, VI) PCz(0.4 μm)/Sn(11 nm), (VII) and as-grown PCz(0.4 μm) films. Scale bars: 1 cm.

Another notable feature in Figure 1 is that the reaction rate using Sn, Ga$_f$, and Ga$_m$ is much faster than that of the reaction using Al. For the Sn, Ga$_f$, and Ga$_m$, a rapid decrease in the absorptions at 680 and 380 nm was observed (spectra a, b, and d in Figure 1) and the reaction was completed in several to several tens of minutes. In the case of Al, the PCz film surface was initially covered with Al and colored gray (see the curve taken at $t = 3$ min in spectra c in Figure 1). The hybridization reaction then slowly proceeded ($t = 15$ min) to form the transparent film in ca. 5 h. This may be due to the formation of a less conductive aluminum oxide. Such a compound should retard the electron transfer from the evaporated Al layer to the PCz film, resulting in the lowering of the hybridization reaction rate. On the other hand, tin oxide and gallium oxide are expected to have an electric conductivity ranging from semiconducting to conductive values. This electric nature makes possible a smooth electron transfer during the hybridization reaction, thus leading to the higher reaction rate. Part A in Figure 3 shows the UV−vis transmission spectra of PCz(0.4 μm)/Sn(11 nm) (a), PCz(0.4 μm)/Ga$_f$(6 nm) (b), PCz(0.4 μm)/Al(6 nm) (c), and PCz(0.4 μm)/Ga$_m$ hybrid films (d). The values of t, defined above, are ca. 12 h for the former three samples and ca. 1 h for the PCz/Ga$_m$ sample. Also shown in the figure is the spectrum of the PCz single film (e). The stoichiometric hybrid films are highly transparent over the 400−900 nm wavelength range. Such highly transparent features were demonstrated by the photographs of PCz(0.4 μm)/Sn(11 nm) (I), PCz(0.4 μm)/Ga$_m$ (II), PCz(0.4 μm)/Al(6 nm) (III), PCz(0.2 μm)/Al(3 nm) (IV), PCz(0.4 μm)/Sn(11 nm) (V and VI), and PCz(0.4 μm) films (VII) in part B in Figure 3. The I, II, III, IV, and VII films were coated on the ITO, and films V and VI were back-coated with a polycarbonate film (see section 2.5). As we would expect, the transparency showed a dependence on the thickness of the hybrid films, which can be seen from the difference in appearance between films III and IV.

3.2. Morphological Features of Hybrid Films.

The previous section presented evidence that the hybrid films are composed of undoped PCz, metal oxides/hydroxides, and perchlorate salts of the metals. The morphological feature of the metal compounds in the films should affect their electrical and electrochemical properties, and hence, observations of the film cross section, combined with EDX microanalyses, were done on the stoichiometric hybrid films. Parts a and d in Figure 4, respectively, show TEM images of the cross-sections of the PCz(0.4 μm)/Sn(11 nm) and PCz(0.4 μm)/Ga$_m$ hybrid films. The thicknesses of the hybrid films were determined by the TEM measurements to be 230−260 nm, being different from the thickness measured by the SEM observation, i.e., 400 nm. This decrease in the film thickness is caused by the preparation procedures of the test sample for the TEM observation (see section 2.3), and indicates densification and consolidation of the matrix during the preparation. Both of the films consist of bright and dark regions, the latter region being dispersed in the former background region. The EDX spectra taken in the bright and dark regions of image a are shown in parts b and c in Figure 4, respectively. The former spectrum exhibited signals of carbon (0.28 keV), but no chlorine signal (2.62 keV). This demonstrates that the bright region is composed of an undoped PCz. On the other hand, the latter spectrum has signals assignable to carbon (0.28 keV), oxygen (0.52 keV), tin (3.44 keV), and chlorine (2.62 keV), indicating that the dark region is the mixture of tin compounds and PCz. The copper signals in the spectra originated from the copper sample holder in the EDX measurements. The signals of gallium may come from contamination due to residual gallium generated during the focused beam ion milling of the sample films with gallium ions. Signal intensities in parts b and c are normalized in such a way that the carbon signals (0.28 keV) are equal. The carbon content in the dark region is smaller than that in the bright region, because the carbon should arise from the PCz. Accordingly, the content of copper may be considered to be the same in both the bright and the dark regions. The EDX spectra taken in the bright (part e) and the dark regions (part f) of image d show that the signals due to chlorine (2.62 keV) and gallium (1.11, 9.25, and 10.36 keV) were mainly detected in the dark region, and drew the analogous conclusion that the gallium compounds are mainly confined to the dark region. In part f of Figure 4, pronounced signals due to In

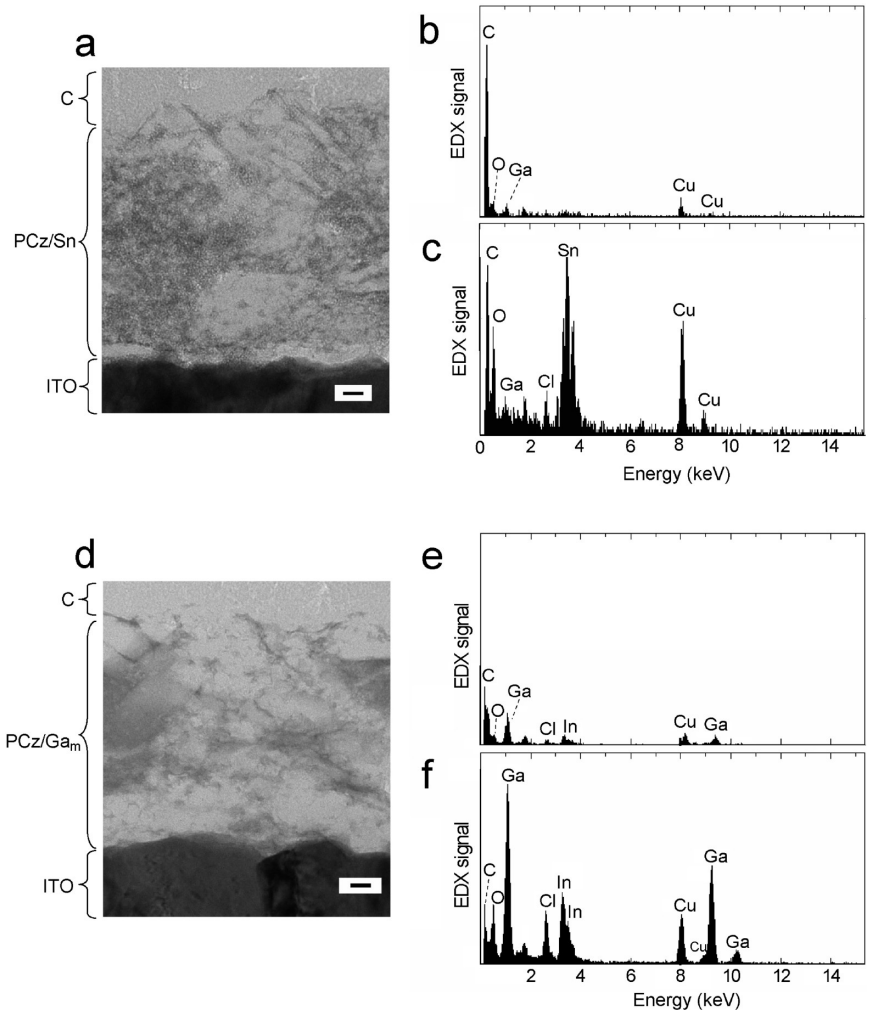

FIGURE 4. TEM images of the cross-section of (a) PCz/Sn and (d) PCz/Ga$_m$ films. (b, c) EDX spectra taken in the bright and dark regions of image a, respectively. (e, f) EDX spectra taken in the bright and dark regions of image d, respectively. Vertical amplitudes of the spectra are normalized by a band of carbon at 0.28 keV. Scale bars: 20 nm.

(3.29 and 3.57 keV) were observed. This is most likely explained by the contamination by indium in the ITO substrate plate and its conversion to indium-gallium-oxides (40−42) during the hybridization reaction.

3.3. Electrochemical Properties. The feasibility of hybrid films for use as an electrochemical electrode was examined by cyclic voltammetry. First, the electrochemical behaviors of the hybrid films attached to the ITO plate were investigated. Electrical contacts were made to the ITO region in which no film was deposited (see part a in Figure 7). Figure 5 shows the cyclic voltammograms of 1 mM Fc in a dichloromethane solution containing 0.1 M TBAP at a PCz(0.4 μm)/Sn(11 nm) film coated on the ITO (a), a PCz(1 μm)/Al(16 nm) film coated on the ITO (b), and a bare ITO (c) at the sweep rate, v, of 20 mV s^{-1}. Voltammograms a and b exhibited a redox wave at a half-wave potential, $E_{1/2}$, of ca. 0.5 V vs SCE which is identified as a redox couple $Fc^{+/0}$ from analogy with the voltammogram c for $Fc^{+/0}$ measured at the bare ITO electrode. Note that both the anodic and cathodic peak currents are nearly the same in magnitude for all the voltammograms. Additionally, the values of the peak separation (ΔE_p) are 180 mV for the PCz/Sn, 220 mV for the PCz/Al, and 200 mV for the ITO electrode. These values are greater than the 60 mV peak separation expected for a reversible electrode reaction and indicated that the above electrode systems are quasi-reversible. In this case, the ΔE_p value is affected by the standard heterogeneous rate constant (k^0), transfer coefficient (α), sweep rate (v), and uncompensated resistance (R_u) (43−45). If we assume that the ΔE_p is nearly independent of α, usually the case for most systems, and resistivity of the hybrid film (R_f) is involved in the value of R_u, the ΔE_p value is a function of k^0 and R_f with v being fixed. Accordingly, comparable values of ΔE_p in the above three systems demonstrates that the hybrid films have a high electroactivity for the electron exchange with a solution species at a film/solution interface under the condition that the films are attached to the electrically conductive plate, and suggest that the films have a high electric conductivity in the film thickness direction.

The high electroactivity of the hybrid films may be related to the intertwined network structure of metal oxides in the films (see the TEM images in Figure 4). In the stoichiometric hybrid films, metal oxides are in contact with each other and provide many electrical pathways for high electroactivity. The electroactivity of the PCz/Al composite seems to be higher than we expected despite the insulating nature of

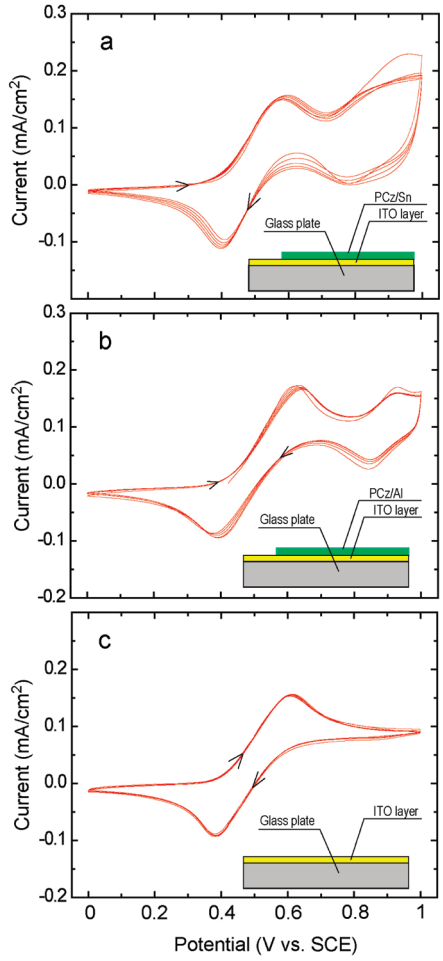

FIGURE 5. Repeated cyclic voltammograms of 1 mM ferrocene in a dichloromethane solution containing 0.1 M TBAP at (a) PCz(0.4 μm)/Sn(11 nm) and (b) PCz(1 μm)/Al(16 nm) hybrid films coated on the ITO plate at the sweep rate of 20 mV s^{-1}. (c) Voltammograms measured at a bare ITO electrode plate for comparison purposes. Cross-sectional structure of the electrode sample is included in each part.

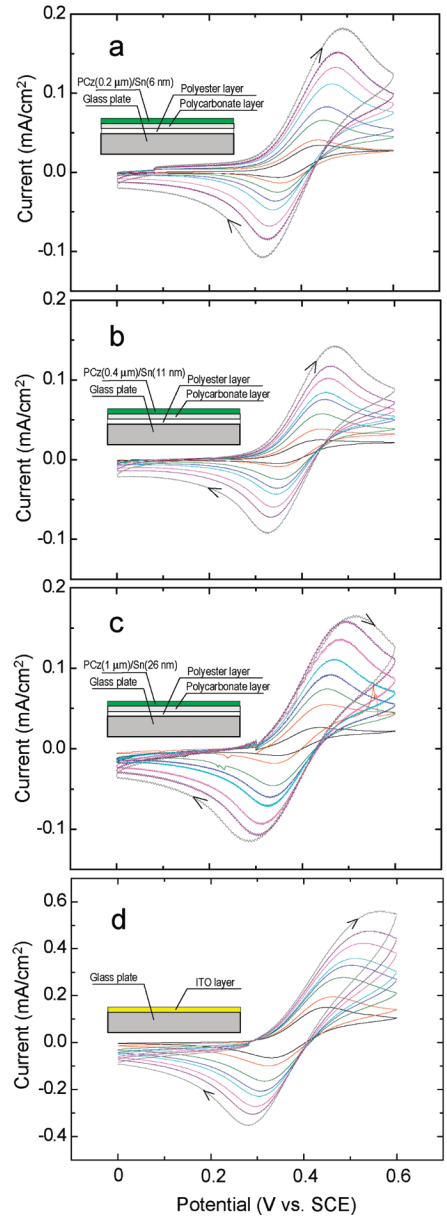

FIGURE 6. Cyclic voltammograms of 1 mM ferrocene in an acetonitrile solution containing 0.1 M TBAP at (a) PCz(0.2 μm)/Sn(6 nm), (b) PCz(0.4 μm)/Sn(11 nm), and (c) PCz(1 μm)/Sn(26 nm) film electrodes at varying sweep rates. The films were stuck to a glass plate by polycarbonate and polyester layers (see the inset in each part). (d) Voltammograms measured at a bare ITO electrode plate for comparison purposes.

aluminum oxide. Although the reason for this is not clear, it is possible to assume that the thus formed aluminum oxide particles contain many imperfections, impurities, and adsorbed water which contribute to the electric conduction (46, 47).

In voltammogram a, the redox wave for $Fc^{+/0}$ is followed by the wave centered at ca. 0.82 V. This was assigned to the doping−dedoping reaction of the PCz/Sn hybrid film on the basis of the cyclic voltammogram of the hybrid film in a blank solution (see the Supporting Information). This wave was also observed in voltammogram b, but it exhibited smaller currents and more anodic potential position than that in voltammogram a. This implies that the PCz/Sn film has a higher electroactivity for the doping−dedoping reaction than the PCz/Al film, the reason of which might be again attributed to the less conductive nature of the aluminum oxide compared to the tin oxide.

Second, the hybrid films were separated from the ITO plate according to the procedure in section 2.6 and their electrochemical behaviors were investigated. Figure 6 shows the cyclic voltammograms of 1 mM Fc in an acetonitrile solution containing 0.1 M TBAP at the PCz(0.2 μm)/Sn(6 nm) (a), PCz(0.4 μm)/Sn(11 nm) (b), and PCz(1.0 μm)/Sn(26 nm) film electrodes (c). The sweep rate was varied from 10 to 300 mV s^{-1}. Included in this figure for comparison are the voltammograms of Fc at the ITO under the same solution and electrolysis conditions (part d in Figure 6). Based on the wave shape and ΔE_p value (Table 1), the electrochemical reversibility at the PCz/Sn film electrodes is rather good and better than that at the ITO. Plots of the anodic peak current for the oxidation of Fc versus square root of v at the PCz/Sn film electrodes gave straight lines intersecting the origin, indicating the diffusion-controlled electrode reaction. These results allowed us to assume that the PCz/Sn films have a

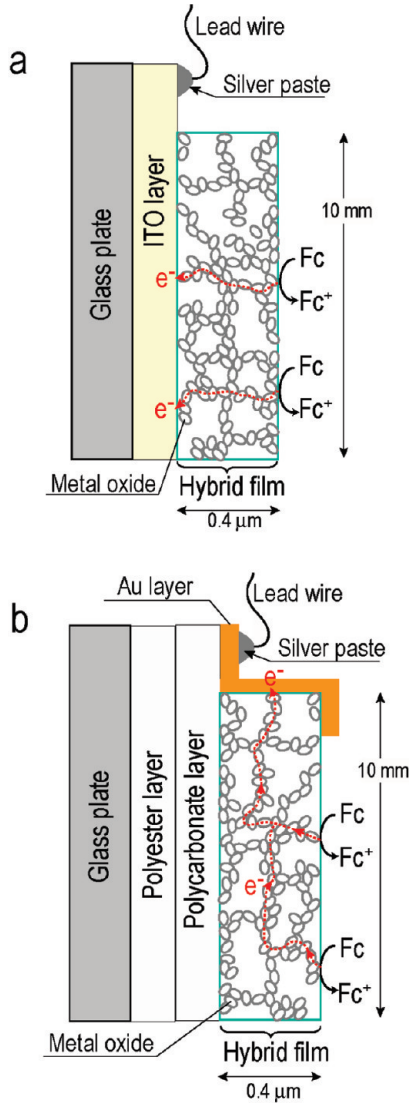

FIGURE 7. Expected structure model for (a) the hybrid films prepared on the ITO plate and (b) the film electrodes prepared by stripping the hybrid films from the ITO (or stainless) plate and sticking them on a glass plate by polycarbonate and polyester layers.

Table 1. Values of ΔE_p and i_{pa} for $Fc^{+/0}$ Redox Couple Measured at the PCz/Sn and PCz/Al Film Electrodes and Compared to an ITO Electrode

electrode	ΔE_p (mV)[a]	i_{pa} (μA)[a]
PCz(0.2 μm)/Sn(6 nm)	73	40
PCz(0.4 μm)/Sn(11 nm)	80	39
PCz(1 μm)/Sn(26 nm)	100	54
PCz(0.6 μm)/Al(10 nm)	90	33
PCz(0.8 μm)/Al(13 nm)	85	37
PCz(1 μm)/Al(16 nm)	100	22
ITO	133	200

[a] Values measured at a sweep rate of 20 mV s^{-1}.

higher compatibility with Fc (presumably higher k^0) than the ITO under the condition that the R_f values for the former and the latter electrodes are comparable. However, the anodic peak current density values, i_{pa}, at the PCz/Sn film electrodes are depressed to ca. one-fifth of those at the ITO at $v = 20$ mV s^{-1}. If this current depression were attributed to the resistive effect of the hybrid films, the ΔE_p values would be greater than that at the ITO electrode. Thus, an account for the simultaneous reduction in the current density and ΔE_p at the hybrid film electrodes should require a specific film structure having anisotropic conductive paths. Schematics a and b in Figure 7 show the expected structure model for the test electrode samples employed in Figures 5 and 6, respectively. These schematics are illustrated on the assumption that the conductive paths in the films are created by a three-dimensional network of conductive metal oxide filler particles and are preferentially formed in the film-thickness direction. In the case of the electrode system in Figure 7a, many conductive paths electrically connect the solution species (Fc) to the current collector (ITO plate), making possible a smooth electron exchange. On the other hand, the conducting path in the in-plane direction is needed for the current flow between the Fc species and the current collector (evaporated Au layer) in the electrode system shown in Figure 7b. The scarcity of the conductive paths in this direction would reduce the effective area of the film electrode, leading to the reduced current density.

To confirm this anisotropic conductivity, we directly measured the conductivity in the in-plane direction ($\sigma_{||}$) and in the film-thickness direction ($\sigma_{\perp}$) using different electrode configurations (48). For the measurement of $\sigma_{||}$, the PCz(0.4 μm)/Sn(11 nm) film system shown in Figure 6b was employed. A comb-shaped gold electrode (Figure 8a) was vacuum evaporated on the film and the current−voltage characteristics was measured with a digital multimeter (Advantest Co., model R8240) using a two probe dc method. On the other hand, for the measurement of $\sigma_{\perp}$, the PCz(0.4 μm)/Sn(11 nm) film system shown in Figure 5a was used. A part of the film prepared on the ITO was dipped in a binder polymer solution composed of polyester (Toyobo Co. Vylon 200, resistivity $\geq 7.2 \times 10^{16}\ \Omega$ cm), toluene, tetrahydrofuran (1:3:3 weight ratio). The sample was pulled out of the solution and dried at 40 °C for 3 h. Then, a gold electrode was evaporated on the resultant film partly covered with the polyester layer (see Figure 8b), and the currents flowing between the ITO and the gold electrodes were measured as a function of the applied bias voltage. The values of $\sigma_{||}$ and $\sigma_{\perp}$ thus determined were 8.4×10^{-10} S cm^{-1} and 1.6×10^{-6} S cm^{-1}, respectively, being the support for the anisotropic conductivity of the hybrid film. Note that the values of $\sigma_{||}$ and $\sigma_{\perp}$ are much lower than the electronic conductivity (σ) measured by the four-point-probe method (see section 3.4) due to the contact resistance (49) between the gold (or ITO) electrode and the hybrid film.

The cyclic voltammetric measurements of Fc were also made using the PCz/Al hybrid film electrode (Figure 9). In this case, the ΔE_p values also indicated that the film electrodes have a higher electrochemical reversibility than the ITO (Table 1). The i_{pa} values are slightly lower than those at the PCz/Sn film electrodes. In view of the anisotropic conduction model in Figure 7, the decreased i_{pa} values led us to assume that the conductive paths in the in-plane direction are smaller in number than those of the PCz/Sn film elec-

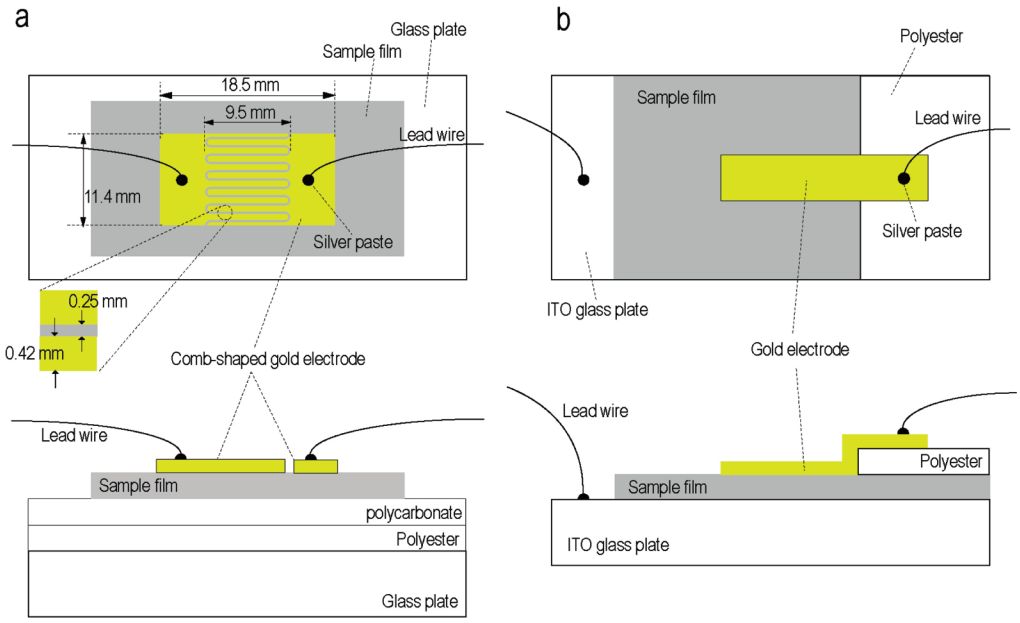

FIGURE 8. Samples and electrode configurations for the measurements of (a) $\sigma_{||}$ and (b) $\sigma_{\perp}$. The lower and upper illustrations show the cross-sectional and plan view of the samples, respectively.

trode. This assumption may be explained by a comparison of the cross-sectional TEM images of the two films. The image of the PCz/Al film was already reported in our previous report (31), but is again demonstrated in the Supporting Information. The comparison clearly demonstrates that the amount of the metal compounds in the PCz/Al film (imaged as a dark region) is lower than that in the PCz/Sn film. Additionally, as was rationalized in section 3.1, the oxide to salt ratio in the former film is lower than that in the latter film. These effects lead to the formation of fewer conductive paths in the in-plane direction, and explain the decreased i_{pa} values of the PCz/Al film electrodes.

3.4. Electric Conductivity. To electrically characterize the hybrid films, electric conductivity (σ) measurements were made while varying the amount of the evaporated metals. Figure 10 shows the dependences of σ (● and ▲) and the absorbance at 680 nm (ABS, ○) on the evaporated metal layer thickness (L) for the PCz/(0.4 μm)/Sn (a), PCz/(0.4 μm)/Al (b), and PCz/(0.4 μm)/Ga_f films (c). The closed circles and triangles show the data for the films prepared on the ITO and the stainless plates, respectively. All the ABS−L plots showed a similar dependence, the decrease in ABS to a minimum at the CFT and its subsequent rise, the reason of which has already been explained in section 3.1. On the other hand, the σ−L plot depended on the type of metal. The σ value almost monotonously increased with L for the PCz/Sn film (part a in Figure 10). In the case of the Al and Ga metals, the σ−L plots showed a dependence similar to their ABS−L plots. This difference in the σ−L relationship can be explained by the difference in the electric conductivity of the generated metal oxide species. Part a in Figure 11 shows a schematic that qualitatively explains the metal-dependent relationship. In the schematic, σ_0 is the electric conductivity of the as-grown ClO_4^--doped PCz film, and line A denotes the conductivity decrease caused by the polymer dedoping reaction. Lines B and C indicate the conductivity change caused by the formation of the metal oxides with good and poor conducting natures, respectively. Above the metal film thickness of the CFT, an excess amount of metal, not participating in the hybridization reaction, should increase the conductivity of the films (line D). In the case of Sn, the σ value would be increased by the high conducting tin oxide filler, so that it can be expressed by the combination of lines A, B, and D, giving a monotonous increase in σ with L (dotted line A + B + D). When the low conducting aluminum oxide or gallium oxide filler is formed, lines A, C, and D may contribute to the electric conduction behavior and gives the relationship denoted by the dashed line A + C + D. This simple model qualitatively well explains the metal-dependent σ−L relationships for the PCz/metal hybrid films. In addition, note that the σ value at the CFT for the PCz/Al (part b in Figure 10) is lower than that for the PCz/Ga_f (part c in Figure 10). This implies that the electric conductivity of the generated aluminum oxide is lower than that of the gallium oxide; hence, the conductivity of the metal oxides generated in the hybrid films is in the increasing order of aluminum oxide < gallium oxide < tin oxide.

The σ value for the stoichiometric PCz(0.4 μm)/Sn(11 nm), PCz(0.4 μm)/Al(6 nm), and PCz(0.4 μm)/Ga_f(6 nm) hybrid films were 6.0×10^{-3}, 2.2×10^{-4}, and 5.2×10^{-4} S cm^{-1}, and are of sufficient conductivity for antistatic applications (7, 9) However, note that these conductivities are the lowest limit. For the electric conductivity measurements, the apexes of the four point probes are brought into contact with a film surface (part b in Figure 11). The σ values measured with this probe arrangement are significantly affected by the conductivity in the in-plane direction. Thus, our PCz/metal hybrid films with few conductive paths in the in-plane direction (see section 3.3) may have a higher conductivity in the thickness direction than the measured σ values.

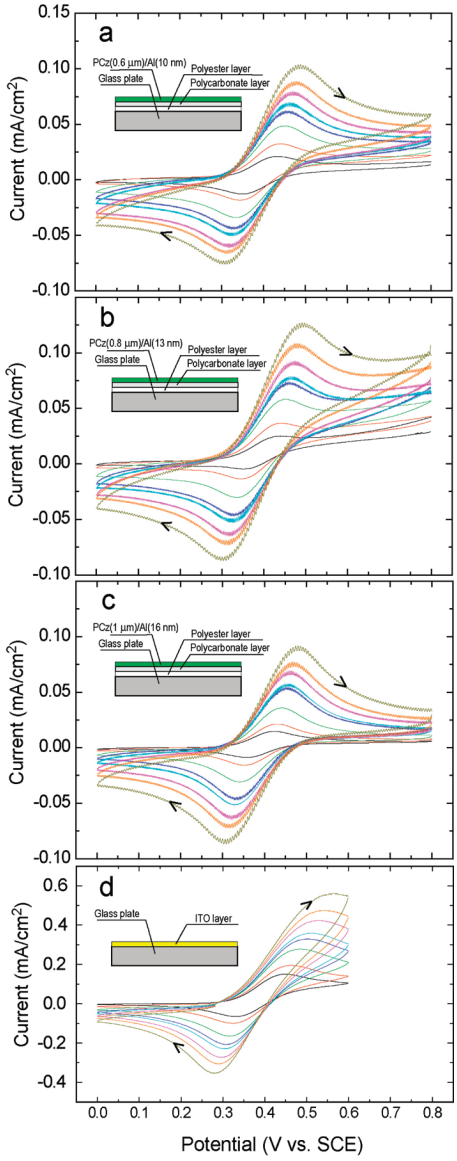

FIGURE 9. Cyclic voltammograms of 1 mM ferrocene in an acetonitrile solution containing 0.1 M TBAP at (a) PCz(0.6 μm)/Al(10 nm), (b) PCz(0.8 μm)/Al(13 nm), and (c) PCz(1 μm)/Al(16 nm) film electrodes at varying sweep rates (see the insets for their cross-sectional structures). Part d shows the voltammograms measured at a bare ITO electrode plate for comparison purposes.

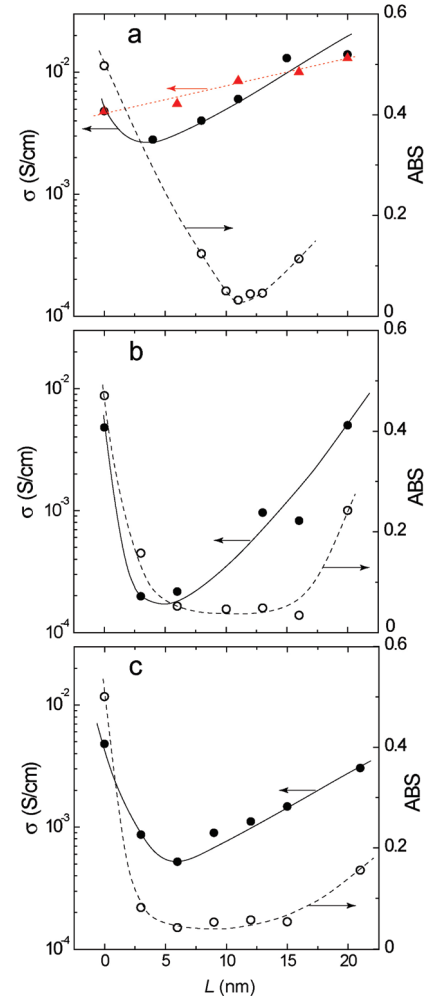

FIGURE 10. Dependences of σ (•) and the absorbance at 680 nm (○), ABS, on the evaporated metal layer thickness (L) for (a) PCz(0.4 μm)/Sn, (b) PCz(0.4 μm)/Al, (c) PCz(0.4 μm)/Ga$_f$ prepared on the ITO plate. Closed triangles show the electric conductivity data for a PCz(0.4 μm)/Sn hybrid film prepared on a stainless plate. In this study, the stainless plate was used exclusively for the preparation of the PCz(0.4 μm)/Sn films.

Figure 12 shows the dependence of σ (part a) and ABS (part b) on contact time for the PCz(0.4 μm)/Ga$_m$ films at 35 (● and ○), 40 (▲ and △), and 60 °C (■ and □). Both of the values of σ and ABS decreased by applying the metals to the PCz film and reached the values of ca. 1×10^{-3} S cm^{-1} and ca. 0.05, respectively, after the contact time of ca. 5 min. The initial decrease in σ can be again explained by the time-dependent progress of the polymer dedoping reaction and the formation of a less conductive gallium oxide. This decrease is undesirable for the practical applications of the hybrid films. Therefore, we are beginning to prepare hybrid films using low-melting metal alloys whose oxides are expected to have high electric conductivity. Part c is the steady-state UV−vis transmission spectra of the PCz(0.4 μm)/Ga$_m$ hybrid films generated at 35 (A), 40 (B), and 60 °C (C). All the films showed a high transmittance in the visible light region, demonstrating that the hybridization reaction can be simply caused by applying metals to the PCz film. Indeed, the reaction also proceeded during the contact between the PCz film on the ITO and a tin film evaporated on a polyester sheet. These results present a simple methodology for the hybridization reaction. Another notable feature of this method is found in the plots of Figure 12: both the σ and ABS values are almost constant after a prolonged contact time. This indicates that no excess amount of Ga remained in the films, and implies that the precise control of the amount of Ga in contact with the PCz is not necessary. This feature is in contrast to the case of the PCz/metal (metal = Sn, Al, and Ga$_f$) systems in which the metal thickness needs to be adjusted to the CFT in order to obtain stoichiometric hybrid films with a colorless transparency.

4. CONCLUSIONS

The preparation and characterization of novel transparent conducting films were reported. Electropolymerized green-colored PCz films reacted with evaporated Sn,

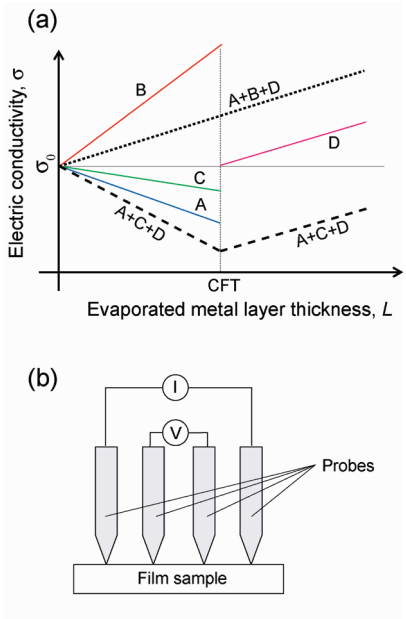

FIGURE 11. (a) Schematic to qualitatively explain the dependences of σ and ABS on L shown in Figure 10. (b) Schematic illustration of the apparatus for the conductivity measurements of the hybrid films by a four-point probe method.

Al, and Ga films and a molten Ga mass in air to form conducting films with a colorless transparency (section 3.1). The transmittance of the resultant hybrid films (0.4 μm thick) ranged from 90 to 95% at a wavelength of 550 nm. This spontaneous solid-state reaction was successfully explained in terms of the combination of a metal corrosion reaction and polymer dedoping reaction (section 3.1). Transmission electron microscopic observations, coupled with an electron-dispersive X-ray analysis, demonstrated that the corrosion products (metal oxides and metal salts) were dispersed in the undoped PCz backbone (section 3.2). The cyclic voltammetry of ferrocene was carried out at the PCz/metal (metal = Sn and Al) films coated on the ITO plate and the PCz/metal (metal = Sn and Al) free-standing film electrodes. The former electrode systems exhibited a well-defined electrochemical response comparable to that at the ITO. However, the current signals from the latter electrode systems were depressed, whereas the electrochemical reversibility was unaltered. These results were explained on the basis of a specific film structure in which conductive paths are preferentially formed in the film-thickness direction rather than in the in-plane direction (section 3.3). Electric conductivity measurements of the stoichiometric PCz/metal (metal = Sn, Al, and Ga_f) films revealed electric conductivities ranging from 2.2×10^{-4} to 6.0×10^{-3} S cm^{-1} (section 3.4). In addition, it was demonstrated that the hybrid films can be simply formed by applying molten metal to the PCz film. The resultant PCz/Ga_m films have an electric conductivity of ca. 1×10^{-3} S cm^{-1} and visible-light transmittance of 90−95% at a wavelength of 550 nm (section 3.4).

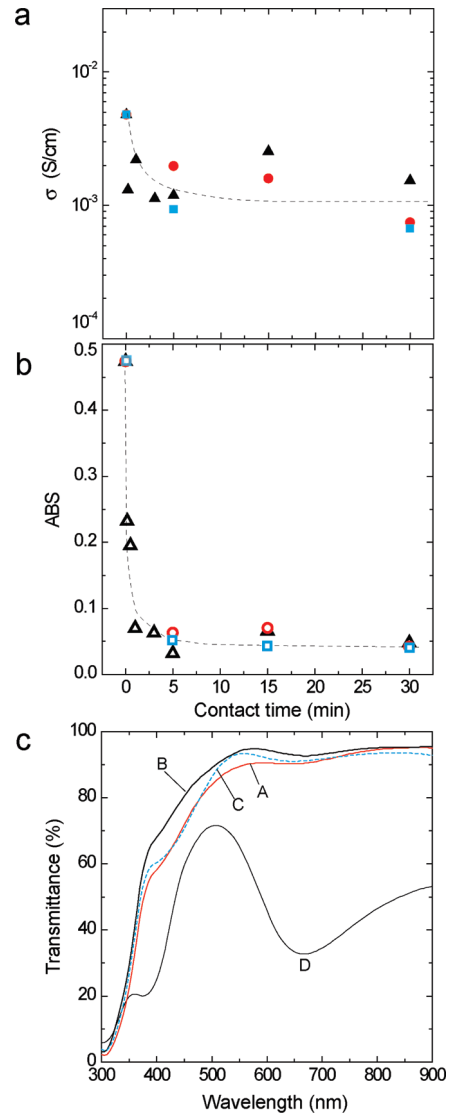

FIGURE 12. Dependences of (a) σ and (b) ABS on contact time for PCz(0.4 μm)/Ga_m films at 35 (circles), 40 (triangles), and 60 °C (squares). Part c shows the UV−vis transmission spectra of PCz(0.4 μm)/ Ga_m hybrid films generated at (A) 35, (B) 40, and (C) 60 °C. Curve D in part c shows the spectrum of the as-grown PCz film (0.4 μm thick) for comparison purposes.

We are beginning to extend this finding to the fabrication of soluble conducting polymer/metal hybrid systems, the details of which will be reported elsewhere.

Acknowledgment. This work was partially supported by a Grant-in-Aid for Scientific Research (C) from JSPS to K.H. (21605003).

Supporting Information Available: Cyclic voltammogram of the PCz/Sn hybrid film in a blank solution and the TEM image of the PCz/Al hybrid film (PDF). This material is available free of charge via the Internet at http://pubs.acs.org.

REFERENCES AND NOTES

(1) Minami, T.; Miyata, T. *Thin Solid Films* **2008**, *517*, 1474–1477.
(2) Minami, T. *Thin Solid Films* **2008**, *516*, 5822–5828.
(3) Minami, T. *Thin Solid Films* **2008**, *516*, 1314–1321.
(4) Park, K. S.; Sato, W.; Grause, G.; Kameda, T.; Yoshioka, T. *Thermochim. Acta* **2009**, *493*, 105–108.

(5) U.S. Geological Survey Mineral commodity Summaries 2008; http://minerals.usgs.gov/minerals/pubs/mcs/.
(6) Ajayan, P. M.; Stephan, O.; Colliex, C.; Trauth, D. *Science* **1994**, *265*, 1212–1214.
(7) Sandler, J.; Shaffer, M. S. P.; Prasse, T.; Bauhofer, W.; Schulte, K.; Windle, A. H. *Polymer* **1999**, *40*, 5967–5971.
(8) Baughman, R. H.; Zakhidov, A. A.; de Heer, W. A. *Science* **2002**, *297*, 787–792.
(9) Bryning, M. B.; Islam, M. F.; Kikkawa, J. M.; Yodh, A. G. *Adv. Mater.* **2005**, *17*, 1186–1191.
(10) Martin, C. A.; Sandler, J. K. W.; Windle, A. H.; Schwarz, M.-K.; Bauhofer, W.; Schulte, K.; Shaffer, M. S. P. *Polymer* **2005**, *46*, 877–886.
(11) Moniruzzaman, M.; Winey, K. I. *Macromolecules* **2006**, *39*, 5194–5205.
(12) Gojny, F. H.; Wichmann, M. H. G.; Fiedler, B.; Kinloch, I. A.; Bauhofer, W.; Windle, A. H.; Schulte, K. *Polymer* **2006**, *47*, 2036–2045.
(13) Moisala, A.; Li, Q.; Kinloch, I. A.; Windle, A. H. *Compos. Sci. Technol.* **2006**, *66*, 1285–1288.
(14) Schmidt, R. H.; Kinloch, I. A.; Burgess, A. N.; Windle, A. H. *Langmuir* **2007**, *23*, 5707–5712.
(15) Watcharotone, S.; Dikin, D. A.; Stankovich, S.; Piner, R.; Jung, I.; Dommett, G. H. B.; Evmenenko, G.; Wu, S.-E.; Chen, S.-F.; Liu, C.-P.; Nguyen, S. T.; Ruoff, R. S. *Nano Lett.* **2007**, *7*, 1888–1892.
(16) Xiang, C.; Pan, Y.; Liu, X.; Shi, X.; Sun, X.; Guo, J. *J. Nanosci. Nanotechnol.* **2006**, *6*, 3835–3841.
(17) Xiang, C.; Shi, X.; Pan, Y.; Guo, J. *Key Eng. Mater.* **2005**, *280*–*283*, 123–126.
(18) Jang, J.; Bae, J.; Yoon, S.-H. *J. Mater. Chem.* **2003**, *13*, 676–681.
(19) Bae, J.; Jang, J.; Yoon, S.-H. *Macromol. Chem. Phys.* **2002**, *203*, 2196–2204.
(20) Kobayashi, M.; Colaneri, N.; Boysel, M.; Wudl, F.; Heeger, A. J. *J. Chem. Phys.* **1985**, *82*, 5717–5723.
(21) Pei, Q.; Zuccarello, G.; Ahlskog, M.; Inganäs, O. *Polymer* **1994**, *35*, 1347–1351.
(22) Onoda, M.; Nakayama, H.; Morita, S.; Yoshino, K. *J. Electrochem. Soc.* **1994**, *141*, 338–341.
(23) Groenendaal, L.; Jonas, F.; Freitag, D.; Pielartzik, H.; Reynolds, J. R. *Adv. Mater.* **2000**, *12*, 481–494.
(24) Lee, K. Y.; Kim, Y. K.; Kwon, O. K.; Lee, J. W.; Shin, D. M.; Kim, D. Y.; Sohn, B. C.; Choi, D. S. *Thin Solid Films* **2000**, *363*, 225–228.
(25) Lee, C. S.; Kim, J. Y.; Lee, D. E.; Joo, J.; Wagh, B. G.; Han, S.; Beag, Y. W.; Koh, S. K. *Synth. Met.* **2003**, *139*, 457–461.
(26) Louwet, F.; Groenendaal, L.; Dhaen, J.; Manca, J.; Lupppen, J. V.; Verdonck, E.; Leenders, L. *Synth. Met.* **2003**, *135*−*136*, 115–117.
(27) Winther-Jensen, B.; Krebs, C. *Sol. Energy Mater. Sol. Cells* **2006**, *90*, 123–132.
(28) Lindell, L.; Burquel, A.; Jakobsson, F. L. E.; Lemaur, V.; Berggren, M.; Lazzaroni, R.; Cornil, J.; Salaneck, W. R.; Crispin, X. *Chem. Mater.* **2006**, *18*, 4246–4252.
(29) Crispin, X.; Jakobsson, F. L. E.; Crispin, A.; Grim, P. C. M.; Andersson, P.; Volodin, A.; van Haesendonck, C.; Van der Auweraer, M.; Salaneck, W. R.; Berggren, M. *Chem. Mater.* **2006**, *18*, 4354–4360.
(30) Watanabe, H.; Kitamura, T.; Hoshino, K. *Electrochem. Solid-State Lett.* **2003**, *6*, D1–D3.
(31) Miyazaki, T.; Kim, S.-K.; Hoshino, K. *Chem. Mater.* **2006**, *18*, 5302–5311.
(32) Verghese, M. M.; Basu, T.; Malhotra, B. D. *Mater. Sci. Eng., C* **1995**, *3*, 215–218.
(33) Tran-Van, F.; Henri, T.; Chevrot, C. *Electrochim. Acta* **2002**, *47*, 2927–2936.
(34) Michaelson, H. B. *J. Appl. Phys.* **1977**, *48*, 4729–4733.
(35) Liu, Y.-C.; Hwang, B.-J. *J. Electroanal. Chem.* **2001**, *501*, 100–106.
(36) González, J. A.; Morcillo, M.; Escudero, E.; López, V.; Otero, E. *Surf. Coat. Technol.* **2002**, *153*, 225–234.
(37) Goddard, H. P. *Mater. Perform.* **1981**, *20*, 9–15.
(38) Müller, B. *Farbe Lack* **1997**, *103*, 24–29.
(39) Budavari, S.; O'Neil, M. J.; Smith, A.; Heckelman, P. E.; Kinneary, J. F. *The Merck Index*; Merck & Co.: Whitehouse Station, NJ, 1991.
(40) Shannon, R. D.; Prewitt, C. T. *J. Inorg. Nucl. Chem.* **1968**, *30*, 1389–1398.
(41) Ivankiv, L. I.; Ketsman, I. V.; Savchyn, V. P.; Balitskii, O. A. *Appl. Surf. Sci.* **2006**, *253*, 1709–1712.
(42) Abe, Y.; Nakayama, T. *Mater. Lett.* **2007**, *61*, 3897–3900.
(43) Nicholson, R. S. *Anal. Chem.* **1965**, *37*, 1351–1355.
(44) Nicholson, R. S. *Anal. Chem.* **1965**, *37*, 667–671.
(45) Bard, A. J.; Faulkner, L. R. *Electrochemical Methods*; Wiley: New York, 1980; Chapter 6.
(46) Cohen, J. *Am. Ceram. Soc. Bull.* **1959**, *38*, 441–446.
(47) Hartmann, W. *Z. Physik.* **1936**, *102*, 709–733.
(48) Miyauchi, S.; Shibasawa, M.; Sorimachi, Y.; Tsubata, I. *Kobunshi Ronbunshu* **1990**, *47*, 255–260.
(49) Hao, Q.; Kulikov, V.; Mirsky, V. M. *Sens. Actuators, B* **2003**, *94*, 352–357.

AM900684E